Mobile Rayleigh Doppler wind lidar based on double-edge technique

Lei Tang (唐 磊)[1*], Zhifeng Shu (舒志峰)[1], Jihui Dong (董吉辉)[1] , Guocheng Wang (王国成)[1], Yongtao Wang (汪永涛)[4], Wenjing Xu (徐文静)[1], Dongdong Hu (胡冬冬)[1], Tingdi Chen (陈廷娣)[2], Xiankang Dou (窦贤康)[2], Dongsong Sun (孙东松)[2], and Hyunki Cha[3]

[1]*Anhui Institute of Optics and Fine Mechanics, Chinese Academy of Sciences, Hefei 230031, China*

[2]*School of Earth and Space Sciences, University of Science and Technology of China, Hefei 230031, China*

[3]*Korea Atomic Energy Research Institute, Daejeon, 305-353 Korea*

[4]*Computer Department, Anhui Finance and Trade Vocational College, Hefei 230031, China*

[*]*E-mail:tanglei_66@163.com*

Received February 5, 2010

We describe a mobile molecular Doppler wind lidar (DWL) based on double-edge technique for wind measurement of altitudes ranging from 10 to 40 km. A triple Fabry-Perot etalon is employed as a frequency discriminator to determine the Doppler shift proportional to the wind velocity. The lidar operates at 355 nm with a 45-cm-aperture telescope and a matching azimuth-over-elevation scanner that provides full hemispherical pointing. To guarantee wind accuracy, a single servo loop is used to monitor the outgoing laser frequency to remove inaccuracies due to the frequency drift of the laser or the etalon. The standard deviation of the outgoing laser frequency drift is 6.18 MHz and the corresponding velocity error is 1.11 m/s. The wind profiles measured by the DWL are in good agreement with the results of the wind profile radar (WPR). Evaluation is achieved by comparing at altitudes from 2 to 8 km. The relative error of horizontal wind speed is from 0.8 to 1.8 m/s in the compared ranges. The wind accuracy is less than 6 m/s at 40 km and 3 m/s at 10 km.

OCIS codes: 120.0120, 140.0140, 280.0280.

doi: 10.3788/COL20100808.0726.

The high accuracy and high resolution wind profiles throughout the troposphere and stratosphere are critical for climate studies, improving forecasting, global pollution tracing, hurricane tracking, and identifying possible hazardous weather conditions for aviation, and so on. Doppler wind lidar (DWL) has demonstrated its capability to provide vertical wind profile of desired accuracy, resolution, and distribution throughout the atmosphere from ground-based and airborne platforms[1]. Thus, some research institutes from America, Europe, and Japan had launched DWL studies during the past half century. Direct detection DWL achieved significant progress for the past twenty years as exemplified by the GLOW system from the National Aeronautics and Space Administration of USA (NASA), GroundWinds system from Michigan Aerospace Corporation (MAC)[2], and so on. However, wind lidar studies in China have just started. Liu *et al.* developed a mobile wind lidar based on incoherent iodine absorption technique, and reported its lower troposphere wind profiles in 2000[3,4].

The double-edge technique retrieves instantaneous wind information by making differential measurements of the Doppler-shifted atmospheric echo and outgoing laser pulse. In this letter, a three-channel etalon composed of two edge channels and one locking channel is used as the frequency discriminator to detect the Doppler shift. The three channels have identical transmission curve shapes and different center frequencies. Constant difference of frequencies is achieved by optically coating the plates of etalon. In contrast to the narrow aerosol backscattered spectrum, the molecular backscattered spectrum is broadened widely by the random motion of the air molecules. Molecular-based double-edge technique uses the two edge channels of the triple etalon located in the wings of the broadened molecular backscattered spectrum to determine the Doppler shift. In the system, the frequency offset of two-edge channels corresponding to the molecular spectrum is designed to be 5.1 GHz. The frequency offset of edge filter 1 and locking filter is set at 1.7 GHz. Thus, the half-height point of locking channel serves as the cross point of the two-edge filters used to lock the outgoing laser frequency[5−7] which is shown in Fig. 1.

Etalon is the key component of DWL. The transmission function for a Fabry-Perot (F-P) etalon at a given frequency, v, is derived over the incident beam divergence angle θ:

$$h(v) = T_{\rm pe}\left[1 + \frac{4F_{\rm e}^2}{\pi^2}\sin^2\left(\pi v\cos\theta/v_{\rm FSR}\right)\right]^{-1}, \qquad (1)$$

where $T_{\rm pe}$ is the peak transmission, $F_{\rm e}$ is the efficient finesse of the etalon, and $v_{\rm FSR}$ is free spectral range.

The normalized Mie- and Rayleigh-scattering spectral functions, $f_{\rm M}(v)$ and $f_{\rm R}(v,{\rm T})$, respectively, have Gaussian profiles[8] represented as

$$f_{\rm M}(v) = (4\ln 2/\pi\Delta v_{\rm M}^2)^{1/2}\exp(-v^2 4\ln 2/\Delta v_{\rm M}^2), \qquad (2)$$

$$f_{\rm R}(v,T) = (4\ln 2/\pi\Delta v_{\rm R}^2)^{1/2}\exp(-v^2 4\ln 2/\Delta v_{\rm R}^2), \qquad (3)$$

where $\Delta v_{\rm M}$ is the full-width at half-maximum (FWHM) of the aerosol backscatter spectrum. This is replaceable

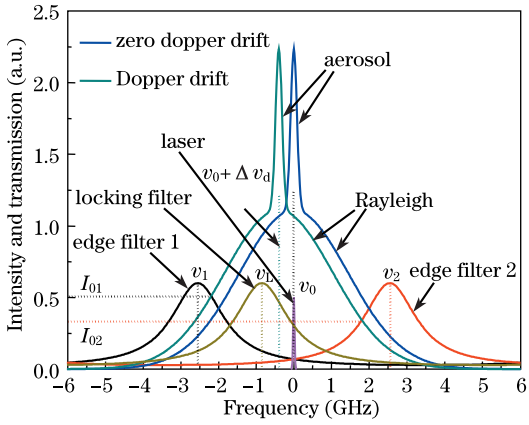

Fig. 1. Spectral profiles of laser, Rayleigh, and Mie scattering signals along with transmission functions.

by the FWHM of outgoing laser spectrum given that the Brownian motion of aerosol particles does not broaden the spectrum significantly. The FWHM of the atmospheric molecular spectrum[9] $\Delta v_{\rm R}$ is represented as

$$\Delta v_{\rm R} = (32kT\ln 2/\lambda^2 M)^{1/2}, \tag{4}$$

where k is the Boltzmann constant, T is the atmospheric temperature, and M is the average mass of an atmospheric molecule. Mie-scattering (or outgoing laser) transmittance and Rayleigh-scattering transmittance at atmospheric temperature T[10] can be written as

$$T_{\rm L}(v) = T_{\rm M}(v) = \int_{-\infty}^{+\infty} h(v-v')f_{\rm M}(v'){\rm d}v', \tag{5}$$

$$T_{\rm R}(v,T) = \int_{-\infty}^{+\infty} T_{\rm M}(v-v')f_{\rm R}(v',T){\rm d}v'. \tag{6}$$

The locking channel transmittance of the outgoing laser is measured by two analog PMT detectors:

$$T_{\rm L}(v_{\rm L}) = a_1 I_{\rm Ls}/I_{\rm Le}, \tag{7}$$

where a_1 is a constant, $I_{\rm Ls}$ is the transmitted signal measured on the locking channel, and $I_{\rm Le}$ is the signal measured on the corresponding energy monitor channel.

When the intensities of the backscattered light incident on the two edge channels of the etalons are assumed to be equal and the two detectors have the same sensitivity, the transmitted signals measured on the two-edge channels are[11,12]

$$I_{01} = a_1\left\{\int_{-\infty}^{\infty} T_{\rm M1}(v-v_1)I_{\rm M}[v-(v_0+\Delta v)]{\rm d}v + I_{\rm R}T_{\rm R1}(v_0+\Delta v-v_1,T)\right\} \tag{8}$$

$$I_{02} = a_2\left\{\int_{-\infty}^{\infty} T_{\rm M2}(v-v_2)I_{\rm M}[v-(v_0+\Delta v)]{\rm d}v + I_{\rm R}T_{\rm R2}(v_0+\Delta v-v_2,T)\right\}, \tag{9}$$

where I_{01} represents the transmitted signals on the one edge channel; I_{02} represents the transmitted signals on another edge channel; a_1 and a_2 are calibration constants; $I_{\rm M}$ and $I_{\rm R}$ are the aerosol backscattered signal and the Rayleigh backscattered signal, respectively; $T_{{\rm M}i}$ and $T_{{\rm R}i}$ $(i = 1,2)$ are the corresponding transmissions; v_0 is the frequency of outgoing laser; Δv is the FWHM of the etalon. The aerosol and the molecular components of the backscattered signal have different spectral characteristics. For this reason, the same sensitivity to molecular and aerosol signals was chosen to eliminate the effect of the aerosol backscattered signals[13], $T_{\rm M1}/T_{\rm M2} = T_{\rm R1}/T_{\rm R2}$. Response function is introduced to detect the relative change in the transmitted signals due to Doppler frequency shift:

$$R(v) = \frac{I_{01}}{I_{02}} = \frac{T_1(v_1+\Delta v_{\rm D},T)}{T_2(v_2+\Delta v_{\rm D},T)}, \tag{10}$$

where T_1 and T_2 are the transmissions of the two edge channels and Δv_D is the Doppler shift. When Δv_D is the single value function of R in wind measurement dynamic range, the line of sight (LOS) wind velocity $v_{\rm r}$ is retrieved using

$$v_{\rm r} = \frac{R(v_0+\Delta v_{\rm D},T)-R(v_0,T)}{R(v_0,T)}\cdot\frac{1}{\theta_v}, \tag{11}$$

$$\theta_v = \frac{2}{\lambda R(v)}\frac{{\rm d}R(v)}{{\rm d}v}, \tag{12}$$

where θ_v is the velocity sensitivity and λ is the laser wavelength.

Four laser beams were pointed to every 90° azimuth sequentially with 30° zenith angle; the first beam was pointed to the east. Photons were accumulated every 3.8 μs corresponding to 570-m LOS range resolution. The radial wind velocities, namely, $v_{\rm rE}$, $v_{\rm rS}$, $v_{\rm rW}$, and $v_{\rm rN}$, were observed clockwise. Wind velocity and direction were retrieved according to the two orthogonal LOS wind velocities.

DWL based on Rayleigh backscatter is an active detection instrument using molecular backscatter to measure wind[10]. Specifically, the molecular backscatter from a laser pulse is collected by telescope, range-gated, and spectrally analyzed to determine Doppler shift, as shown in Fig. 2. The system consisted of four major subsystems, including the laser transmitter subsystem, the scanning telescope (transceiver) subsystem, the receiver subsystem, and the controlling subsystem. The transmitter was a 355-nm injection-seeded Nd:YAG laser, which produced the output laser beam at 355 nm to take advantage of the λ^{-4} dependence of the molecular backscatter. The outgoing laser beam was directed through a 10× expander to compress the beam divergence to less than 0.1 mrad. Prior to laser beam directing, a very small fraction of the outgoing laser was coupled directly into the receiver through a 100-μm-diameter multimode fiber. This was used as the reference signal to determine its frequency. The transceiver optical system consisted of a 45-cm-aperture Cassegrain telescope and a matching azimuth-over-elevation scanner that can provide full hemispherical pointing. The backscattered signal that

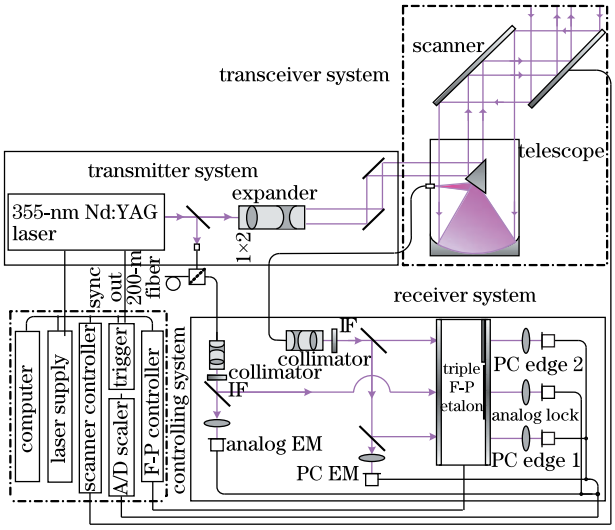

Fig. 2. Schematic of the lidar system. PC: photon counting; EM: energy monitor.

carried Doppler-shift information was collected and focused into a 200-μm-diameter multimode fiber to couple the signal from the telescope to the receiver[14].

In the receiver, the reference light was coupled to a collimator to produce a collimated beam with diameter of 18 mm. After passing through an interference filter (IF) with the bandwidth of 0.15 nm at 355 nm, the reference light was split into two channels by a beam splitter. The transmitted light with 77% of the reference light illuminated the locking channel of the triple Fabry-Perot etalons. The signals that passed through the etalon were then coupled into an analog mode photomultiplier tube (PMT). The reflected light with 23% of the reference light was detected by another analog mode PMT. The signals collected by two analog detectors were then sampled to determine the outgoing laser frequency. The backscattered light was coupled to another collimator to produce a collimated beam with a diameter of 36 mm. After passing through an IF, the backscattered light was split into three channels by two beam splitters. Two of the light beams with 47% intensity were incident to the two edge channels of the etalons, which provided the information used in the Doppler shift measurement. Another beam with 6% of backscattered light served as the energy monitor channel used to provide intensity normalization of the respective etalon channels during calibration. The three backscattered-light channels were detected by three photon-counting PMT for the very weak backscattered light. The laser operation, Fabry-Perot interferometer (FPI) spacing parallelism, data collection, and X-Y scanner orientation were controlled by an industrial computer. Software was developed to achieve real-time signal processing and unattended operation[15]. The system parameters are summarized in Table 1.

Stepping through the timing for a single laser pulse could help us understand how the different signals were collected, as shown in Fig. 3. The SYNC signal from the laser was used to synchronize the ranged-gating electronics, a programmable circuit consisting of field programmable gate array (FPGA) and microprogrammed control unit (MCU). The trigger signal was sent to analog-to-digital (A/D) multiscaler, photon counting multiscaler, and three photon-counting detectors. The output of the photon-counting detectors was disabled when a low level of transistor-transistor logic (TTL) was applied to its gate input. Thus, the trigger to the photon-counting detectors was used to eliminate the strong atmospheric backscatter from the lower troposphere, where the aerosol concentration is extremely high. The strong signal from the aerosol backscatter made the photon-counting detectors run in the range of nonlinearity, thus decreasing the accuracy of the wind measurement.

The careful calibration of the transmission curve is very important to wind measurement before operation. To measure the etalon transmission curves, the beam splitter placed before the expander (Fig. 1) was replaced by a beam splitting prism to obtain two laser beams, which were used to scan three transmission curves. One was coupled into the receiver by a 100-μm-diameter multimode fiber and used to scan the locking channel. The other was coupled into the receiver by another 200-μm-diameter multimode fiber and used to scan the two edge channels. The two laser beams illuminated the mirror plate of etalon after they were collimated to 18 and 36 mm using two collimators, respectively. The shape of the collimated beam passing through the etalon is shown in Fig. 4. Consecutive changing intensities of the light illuminated on the three channels are likewise shown. Figures 4(a), (b), and (c) show the peaks of edge 2, locking, and edge 1 channels, respectively. Locking etalon peak was located closer to the edge filter 1 peak, ensuring that the frequency of outgoing laser was locked at the center of the two edge channels.

A capacitance bridge fabricated on the mirror plates of the tuning etalon was used to sense changes in parallelism and cavity spacing. Three piezoelectric actuators were used to tune the cavity spacing and permit elimination of parallelism errors. This facilitated convenient and simultaneous measuring of the three transmission curves by scanning the cavity spacing through a spectral range

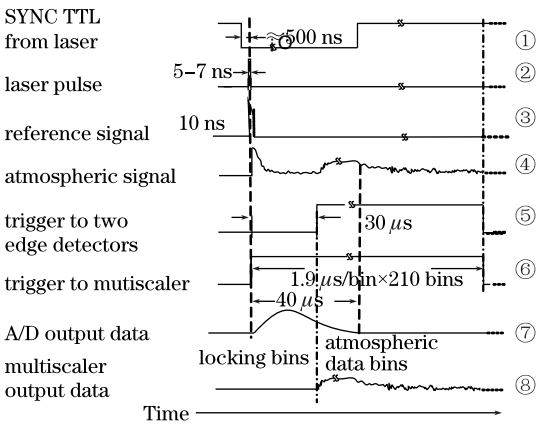

Fig. 3. Data acquisition timing sequence.

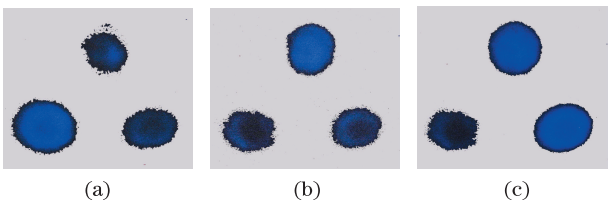

(a) (b) (c)

Fig. 4. Illumination patterns of light passing through triple-channel etalon.

within 12 GHz. A 12-bit digital-to-analog (D/A) converter was used to tune 335-nm cavity spacing, which achieved 5.54-MHz frequency shift per step, corresponding to 0.082-nm cavity spacing changes. Pulsed laser was also used to measure the transmission curves. Five array raw data, including $I_1(v_n)$, $I_2(v_n)$, $I_e(v_n)$, $I_{Ls}(v_n)$, and $I_{Le}(v_n)$ (n is sampling steps), were obtained simultaneously. The three transmissions, namely, $T_1(v_n)$, $T_2(v_n)$, and $T_L(v_n)$, were calculated according to

$$T_1(v_n) = a_1 \frac{I_1(v_n)}{I_e(v_n)}, \quad T_2(v_n) = a_2 \frac{I_2(v_n)}{I_e(v_n)},$$
$$T_L(v_n) = a_3 \frac{I_{Ls}(v_n)}{I_{Le}(v_n)}, \tag{13}$$

where a_1, a_2, and a_3 are calibration constants; I_1, I_2, and I_e are the signals and energy of the two edge channels, respectively. Dots corresponding to the sizes of transmissions are shown in Fig. 5. These dots were fitted by the nonlinearity least two multiplication method. The fitted equation is the theoretical function of transmission[15]:

$$T_M(v) = C + \eta_{FP}\left\{1 + 2\sum_{n=1}^{50} R_e^n \cos\left[\frac{2\pi n(v - v_p)}{v_{FSR}}\right] \cdot \exp\left[-\left(\frac{\pi n \Delta v_l}{v_{FSR}}\right)^2\right] \mathrm{sinc}\left(\frac{2nv_0}{v_{FSR}} \frac{1 - \cos\theta_0}{1 + \cos\theta_0}\right)\right\}, \tag{14}$$

where C is background constant, η_{FP} is the optical efficiency of etalon, $v_l = \delta v/(4\ln 2)^{1/2}$ with δv being the FWHM of laser spectra, the fitted parameters are center frequency v_p, free spectral range v_{FSR}, efficient reflectivity R_e, and peak transmission T_{pe}. These are also shown in Fig. 5.

The results of the nonlinearity fitting show that FWHM of the two edge channels are slightly wider by 5.2% than the theoretical design value. This could be attributed to the divergence angle of the incident beam and the optical coating technique. The FWHM of the locking channel was 1.71 GHz in the admitted error, but peak transmission was shorter than the two edge channels. The fraction of the light passing through etalon was shaded by an outshoot of metal in the light path due to the deficiency of design. However, this did not bring serious effect to wind measurements because it had a sharp slope used to determine outgoing laser frequency.

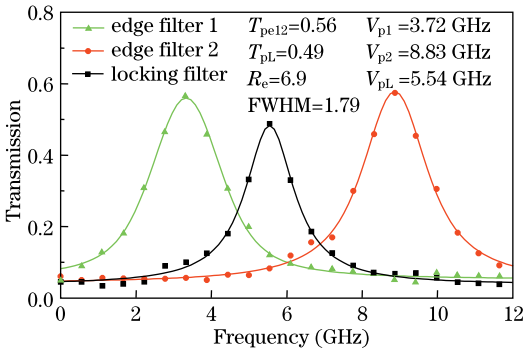

Fig. 5. Scanned and fitted transmission curves.

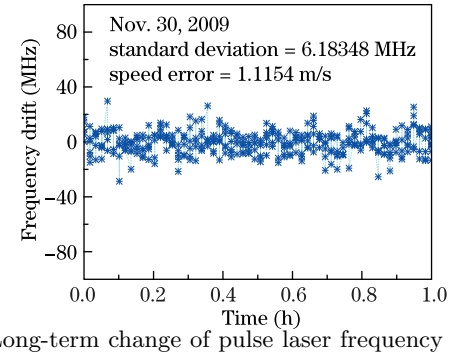

Fig. 6. Long-term change of pulse laser frequency with feedback.

In order to guarantee wind accuracy, a single servo loop was used to monitor the outgoing laser frequency and remove inaccuracies due to the frequency drift of the laser or the etalon. Actively locking the laser and the etalon at the half-height point on the locking filter ensured symmetry of the edge-filter channels for wind measurement. Therefore, the frequency of the outgoing laser could always be locked at the half-height point with high sensitivity. Figure 6 shows the result of the real-time frequency tracking. The standard deviation of the outgoing laser frequency drift was 6.18 MHz, and the corresponding velocity error was 1.11 m/s. The frequency of outgoing laser was always kept near the cross point with high sensitivity.

Comparison experiments between the DWL and the wind profile radar (WPR, Airdal 6000) were held on the same location on the mornings of Dec. 5, 2009 and Dec. 19, 2009. The principal goal was to compare horizontal wind profiles from the WPR and the DWL operated almost coincidentally in space and time. The wind speed and direction accuracies of WPR were expected to be better than 1 m/s and 10°, respectively, with about 250-m spatial resolution and 10-min temporal resolution. The first one was made specifically to compare DWL with WPR in the 1 – 8 km altitude wind profile per 10 min. Thus, the laser pulse energy was reduced, and the four directions were started for 2 min with 250-m range resolution and 3600 shots, for every 90° azimuth sequential with a 60° zenith angle. Wind speed and direction showed good consistency. The maximum wind speed discrepancy was 1.2 m/s at about 3.5-km altitude and direction discrepancy of 9°. The minimum wind speed discrepancy was 0.1 m/s. The rest of the results are shown in Fig. 7(a).

We also conducted comparison experiment of wind measurements from 22:00 PM Dec. 18, 2009 to 05:00 AM of the following day. During the experiment, the three photo-counting PMTs were binned with about 250-m range resolution below the altitude of 20 km and binned again with about 500-m range resolution above the altitude of 20 km. It was integrated for 12600 shots in 7 min at each LOS. The four direction radial wind profiles were combined to retrieve the horizontal wind speed and direction every 30 min. The temporal resolution of the WPR was changed to wind profiles per 30 min and 250-m range resolution. Figure 7(b) shows a summary of comparison of wind speed and direction from 2 to about 8 km, as affected by the limitation of WPR. The wind speed and direction data from the DWL and the WPR were in good agreement from 2 to 8 km, although differences

between the two results were observed. The difference of wind speed and direction at the altitude of 2 km could be due to the nonlinearity of the detectors operating in photon-counting mode. Wind speed error ranged from 0.8 m/s at about 3 km to 1.3 m/s at about 8 km. The maximum values of discrepancy were 1.8 m/s and 16° in the compared range of 2 – 8 km for wind speed and direction, respectively. These discrepancies included both instrumental effects and atmospheric variability during the 30-min measuring period. Given that the meteorological conditions were relatively stable during the experiment, the results of comparison were useful for examining the instrumental errors.

Following the comparison experiment, theory analysis comparing experiment results was also performed. The error from the signal-to-noise ratio (SNR) is typically dominated by the error in the atmospheric component of the differential normalized signal measurement. For the case of a moderately high SNR in both the edge and the energy monitor channels, the noise in the measurement may be considered uncorrelated, and the composite SNR can be given as:

$$\mathrm{SNR} = \left[\mathrm{SNR}_1^{-2} + \mathrm{SNR}_2^{-2}\right]^{-1/2}, \qquad (15)$$

where SNR_1 and SNR_2 are the SNR terms for the measurement of the atmospheric backscattered signal by both the edge filters[16]. The SNR calculated using Eq. (15) is shown in Fig. 8. As can be seen, the SNR decreased along with the increasing altitude, above the black line of 25 at 40 km. The measurement sensitivity is defined as the fractional change in the normalized signal for a unit velocity, as given by Eq. (12). Figure 9 shows the sensitivity of the LOS wind speed from the atmospheric backscattered signal, and the value is 0.65% for small Doppler shift at the atmospheric temperature of 226.5 K. In Fig. 10, the reciprocal of multiplying the sensitivity by the SNR equals the wind measurement error. Theoretical analysis and simulation showed that wind accuracy was less than 6 m/s at 40 km and 3 m/s at 10 km, respectively. The results of experiment entirely accorded with the requirement of design.

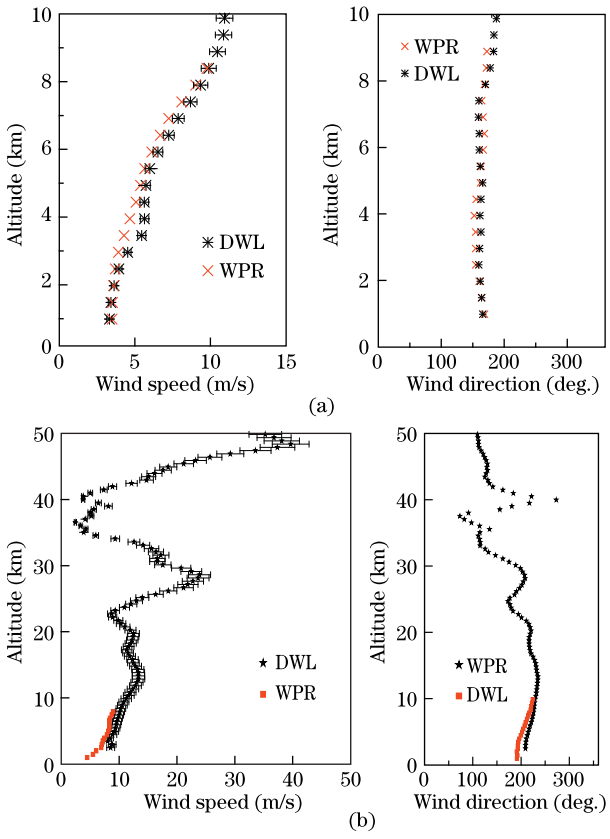

Fig. 7. Horizontal wind speed and direction profiles measured by DWL and WPR on (a) Dec. 5, 2009 and (b) Dec. 19, 2009.

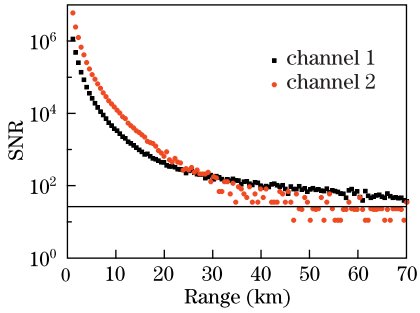

Fig. 8. SNR distributions of signals from edge channels 1 and 2.

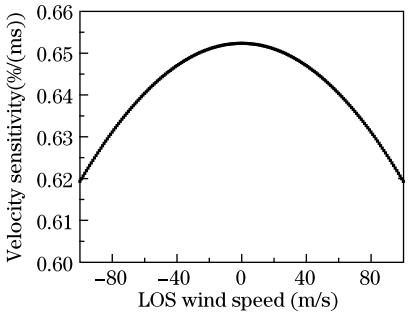

Fig. 9. Sensitivity of wind measurement at 226.5 K.

The DWL finished the prophase observation of stratosphere wind profiles in field operation and obtained some data of wind field observation. Figure 11 shows two examples of the horizontal wind speed and direction obtained on Dec. 21, 2009 at 02:28 AM and 02:58 AM, respectively. The minimal change in wind speed from 10 to 40 km in half an hour and the substantial wind speed change above 40 km may have been due to the lower SNR. The wind direction was stable at high altitude from 15 to 40 km but changed to about 50° at 10 km. The wind profiles of lidar showed a mid-level jet at around 27 km with a local maximum speed of 18 m/s. A second higher-level jet was observed with a speed of nearly 40 m/s above 40 km. A local minimum of 6 m/s in the wind speed was observed at about 40 km (Fig. 11(a)) and 2 m/s at about 39 km (Fig. 11(b)). A wind shear resulted in fluctuation in wind speed and direction at 35 – 40 km, as shown in Fig. 7(b). Some regularity of wind speed and direction changing at troposphere and stratosphere in the consecutive operation was thus observed.

In conclusion, we develop a 355-nm Rayleigh Doppler wind lidar system based on the double-edge technique. Despite the absence of result from higher altitude experiments, we successfully demonstrate the operation of the system. Lidar measured profiles of

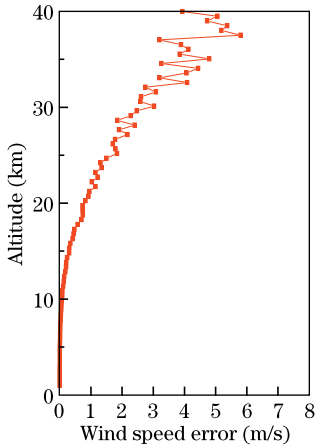

Fig. 10. Wind speed error distribution.

Table 1. Rayleigh Doppler Lidar System Parameters

	Parameter	Value
Transmitter	Wavelength	355 nm
	Laser Linewidth	200 MHz at 355 nm
	Laser Energy Per Pulse	400 mJ
	Laser Repetition Frequency	30 Hz
Transceiver	Telescope/Scanner Aperture	45 cm
	Field of View	0.2 mrad
	Optical Efficiency	$> 85\%$
	Scan Range	$360° \times 90°$
	Filter Bandwidth	0.15 nm
	Filter Peak Transmission	$> 40\%$
Receiver	Etalon Free Spectral Range	12 GHz
	Etalon FWHM	1.7 GHz
	Edge Channel Separation	5.1 GHz
	Locking Channel Separation	1.7 GHz
	Etalon Peak Transmission	60%
	CPM Quantum Efficiency	21%

CPM: channel photomultiplier

wind speed and direction are obtained in altitudes of more than 40 km. In addition, the horizontal wind profiles measured by DWL are consistent with concurrent WPR observations in low altitude. Theoretical analysis of experiment results has validated the performance of the lidar. Good agreement is obtained between the validation data and the requirement of design. Continuous operation of the lidar provides horizontal and vertical information of the wind field, and atmospheric dynamics are observed in the continuous operation. Therefore, this lidar system is able to yield troposphere and stratosphere wind measurements routinely with an accuracy of less than 3 m/s at 10 km and 6 m/s at 40 km, respectively.

This work was supported by the National "863" Project of China and the International Cooperative Project of Anhui Province (No. 09080703032).

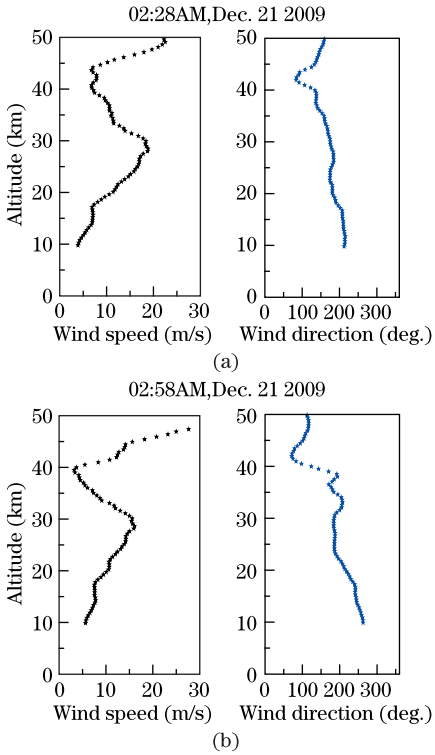

Fig. 11. Wind speed and direction measured by DWL.

References

1. H. Xia, D. Sun, Y. Yang, F. Shen, J. Dong, and T. Kobayashi, Appl. Opt. **46,** 29 (2007).
2. C. Flesia, C. L. Korb, and C. Hirt, Opt. Lett. **25,** 1466 (2000).
3. Z. Liu, Z. Li, B. Liu, and R. Li, Chin. Opt. Lett. **7,** 1051 (2009).
4. Z.-S. Liu, D. Wu, J.-T. Liu, K.-L. Zhang, W.-B. Chen, X.-Q. Song, J. W. Hair, and C.-Y. She, Appl. Opt. **33,** 7079 (2002).
5. C. Souprayen, A. Garnier, A. Hertzog, A. Hauchecorne, and J. Porteneuve, Appl. Opt. **38,** 2410 (1999).
6. C. Souprayen, A. Garnier, and A. Hertzog, Appl. Opt. **38,** 2422 (1999).
7. B. M. Gentry, H. Chen, and S. X. Li, Opt. Lett. **25,** 1231 (2000).
8. M. J. McGill, W. R. Skinner, and T. D. Irgang, Appl. Opt. **36,** 1253 (1997).
9. V. J. Abreu, Appl. Opt. **18,** 2992 (1979).
10. C. L. Korb, B. M. Gentry, S. X. Li, and C. Flesia, Appl. Opt. **37,** 3097 (1998).
11. D. J. McCleese and J. S. Margolis, Appl. Opt. **22,** 2528 (1983).
12. D. Rees and I. S. McDermid, Appl. Opt. **29,** 4133 (1990).
13. M. J. McGill and J. D. Spinherne, Opt. Eng. **37,** 2675 (1998).
14. F. Shen, H. Cha, D. Sun, D. Kim, and S. O. Kwon, Opt. Rev. **15,** 204 (2008).
15. F. Shen, H. Cha, J. Dong, D. Kim, D. Sun, and S. O. Kwon, Chin. Opt. Lett. **7,** 503 (2009).
16. C. L. Korb, B. M. Gentry, and S. X. Li, Appl. Opt. **36,** 5976 (1997).